Ultrathin hexagonal SnS$_2$ nanosheets coupled with g-C$_3$N$_4$ nanosheets as 2D/2D heterojunction photocatalysts toward high photocatalytic activity

Zhenyi Zhang [a], Jindou Huang [a], Mingyi Zhang [b], Qing Yuan [a], Bin Dong [a,*]

[a] School of Physics and Materials Engineering, Dalian Nationalities University, Dalian 116600, PR China
[b] Key Laboratory for Photonic and Electronic Bandgap Materials, Ministry of Education, School of Physics and Electronic Engineering, Harbin Normal University, Harbin 150025, PR China

ABSTRACT

In this work, we present the 2D/2D type of heterojunction photocatalysts fabricated by horizontal loading ultrathin hexagonal SnS$_2$ nanosheets on g-C$_3$N$_4$ nanosheets through a facile ultrasonic dispersion method. The sheet-like structures of these two nanomaterials induce a large contact region in the heterojunction interface, as evidenced by electron microscopic analyses. By taking advantage of this feature, the as-fabricated SnS$_2$/g-C$_3$N$_4$ heterojunction nanosheets exhibit considerable improvement on the photocatalytic activities for the degradation of organic dyes and phenols under visible light irradiation as compared to pure g-C$_3$N$_4$ and SnS$_2$ nanosheets. In particular, the optimal heterojunction nanosheet with 5.0 wt.% SnS$_2$ shows the apparent rate constant of ~0.2 min^{-1} for the RhB photodegradation, which is higher than that of pure g-C$_3$N$_4$ and SnS$_2$ nanosheets by a factor of 4 and 8, respectively. Further studies by steady-state and transient photoluminescence spectroscopy indicate that the photosynergistic effect of SnS$_2$/g-C$_3$N$_4$ heterojunction can remarkably enhance the photoinduced interfacial charge transfer, thereby increasing the charge separation during the photocatalytic reaction.

1. Introduction

Photocatalytic degradation of organic pollutants by using high-performance nanostructured semiconductors has been recognized as one of the most promising strategies to create the clean and comfortable environment for human beings in modern society [1]. As a typical semiconductor photocatalyst, TiO$_2$ has been extensively investigated for the elimination of organic pollutants in the environment over the last few years [2–4]. However, the practical application of this material is still hindered by its main disadvantage of wide band gap (~3.2 eV for anatase), resulting in only a small ultraviolet (UV) fraction (~4.0%) of solar spectrum that can be used to initiate photochemical reactions [5–7]. In order to more efficiently utilize solar energy, a variety of visible-light-responsive semiconductors are being developed as the future generation of photocatalysts, among which carbon based materials are the most popular ones because they are stable, environmentally friendly and abundant [8–10].

Since Wang et al. discovered the photocatalytic water splitting over a metal-free polymeric material, named graphitic carbon nitride (g-C$_3$N$_4$), in 2009, this kind of carbon-based material has attracted much attention in the fields of solar-to-fuel conversion and photocatalytic degradation of environmental pollutants [11–13]. Pure g-C$_3$N$_4$ nanomaterial possesses a two-dimensional (2D) layered structure. The π-conjugated graphitic planes constructed by the sp^2 hybridization of the carbon and nitrogen lead to the narrow band gap (~2.7 eV) and high chemical stability of g-C$_3$N$_4$. The weak van der Waals interaction between the adjacent conjugated planes restricts the electron coupling between the planes. Although the band gap and absolute potentials of g-C$_3$N$_4$ have been proven to be suitable for the photocatalytic reaction by the density functional theory (DFT) calculations, its narrow absorption band and poor quantum yield often result in a low photocatalytic activity [14,15]. Research found that the g-C$_3$N$_4$-based heterojunction could obviously enhance the photocatalytic activity through extending the photoresponding range and increasing the charge separation efficiency. To date, a large number of semiconductors with different nanostructure including nanospheres, nanorods and nanosheets have been coupled with g-C$_3$N$_4$ to advance this 2D photocatalytic material [16–23]. In the view of geometry, there are three types of g-C$_3$N$_4$-based heterojunctions,
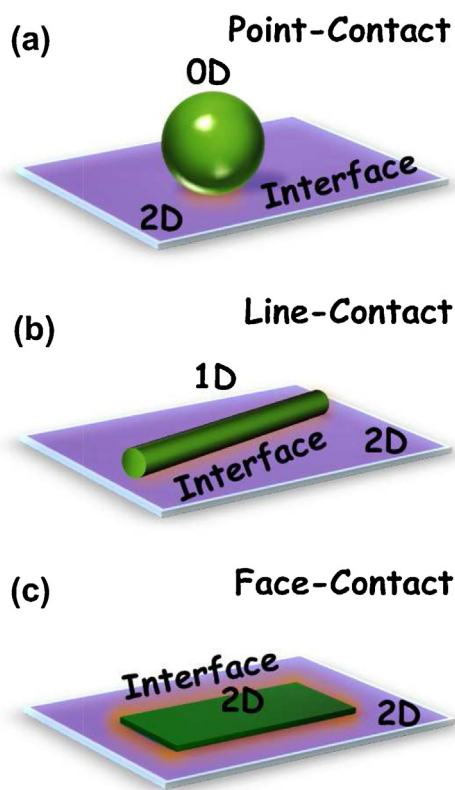
Scheme 1. Schematic diagram of contact interfaces of (a) 0D/2D, (b) 1D/2D, and (c) 2D/2D heterojunction.

called "0D/2D", "1D/2D", and "2D/2D" heterojunction. Among them, the 2D/2D type of g-C$_3$N$_4$-based heterojunction often exhibits the higher charge mobility and low charge recombination rates because its face-to-face contact might form the larger interface region as compared to the point-to-face contact in the 0D/2D heterojunction and the line-to-face contact in the 1D/2D heterojunction (Scheme 1).

Herein, in this work, we gave a successful attempt to construct the 2D/2D heterojunction photocatalysts through coupling the g-C$_3$N$_4$ nanosheets with ultrathin hexagonal SnS$_2$ nanosheets by a facile ultrasonic dispersion process. As a kind of n-type semiconductor, SnS$_2$ nanosheets with a narrow band gap of ~2.48 eV also have a layered structure, which are well-known for their potential applications in the area of photocatalysis in recent years [24–26]. Notably, the SnS$_2$ and g-C$_3$N$_4$ nanosheets have matching band potentials to form the heterojunction. Therefore, horizontal loading ultrathin hexagonal SnS$_2$ nanosheets onto g-C$_3$N$_4$ nanosheets may allow effective photoinduced interfacial charge transfer by taking advantage of intimate face contact. As such, the as-fabricated SnS$_2$/g-C$_3$N$_4$ heterojunction nanosheets exhibit significant enhancement on the photocatalytic activities for the degradation of organic dyes and phenols under visible light irradiation as compared to pure g-C$_3$N$_4$ and SnS$_2$ nanosheets. This enhanced photocatalytic activity is discussed in terms of the highly effective charge separation based on the photosynergistic effect, as confirmed by the steady-state and transient photoluminescence spectroscopy.

2. Experimental

2.1. Fabrication of SnS$_2$/g-C$_3$N$_4$ heterojunction nanosheets

First, the ultrathin hexagonal SnS$_2$ nanosheets were synthesized by a hydrothermal method. Briefly, 0.125 mmol of SnCl$_4$·5H$_2$O and 1 mmol of thioacetamide (TAA) were dispersed in 20 mL of deionized water. After stirring for 30 min, the above mixture was transferred into a Teflon-lined stainless steel autoclave with a capacity of 25 mL. Subsequently, the autoclave was sealed and maintained at 160 °C for 12 h in an electric oven. After hydrothermal reaction, the autoclave was air-cooled to room temperature. The yellow suspension was collected, washed with ethanol and deionized water several times, and finally dried in a vacuum oven at 60 °C for 8 h. Thus, the ultrathin hexagonal SnS$_2$ nanosheets were formed. The graphitic carbon nitride (g-C$_3$N$_4$) was synthesized by a traditional thermal polymerization method. In a typical process, 10 g of urea powder was grounded for 30 min in a mortar and then transferred to an alumina crucible with a cover. Afterward, the crucible was heated to 550 °C with a rising rate of 20 °C min^{-1} and kept for 2 h at the required temperature under semiclosed environment, resulting in the bulk g-C$_3$N$_4$ with faint-yellow color.

SnS$_2$/g-C$_3$N$_4$ heterojunction nanosheets were fabricated by horizontal loading of ultrathin hexagonal SnS$_2$ nanosheets on g-C$_3$N$_4$ nanosheets through a facile ultrasonic dispersion method. A measured amount of as-synthesized bulk g-C$_3$N$_4$ was grounded to fine powder and then added into 40 mL of methanol. After ultrasonic treatment for 30 min, the bulk g-C$_3$N$_4$ was exfoliated into the very thin sheets and disintegrated into a homogeneous suspension. Subsequently, the ultrathin hexagonal SnS$_2$ nanosheets were dispersed in this suspension via an ultrasonic process, and then stirred at room temperature for 36 h. The residual methanol was removed by a stream of nitrogen. At last, the obtained yellow powder was dried in a vacuum oven at 60 °C, and then sealed into a Teflon-lined stainless steel autoclave at 140 °C for 6 h to further consolidate the heterojunction interface. The SnS$_2$/g-C$_3$N$_4$ heterojunction nanosheets were denoted as SCHNX in which X is the nominal weight ratios of SnS$_2$ to g-C$_3$N$_4$ nanosheets. In our present work, the SCHN0.5, SCHN1, SCHN3, SCHN5, and SCHN10 were fabricated to investigate the optimal heterojunction photocatalyst. Meanwhile, the pure SnS$_2$ and g-C$_3$N$_4$ nanosheets as the control samples were also synthesized.

2.2. Characterization

X-ray diffraction (XRD) patterns of the as-synthesized samples were recorded by a Shimadzu XRD-600 X-ray diffractometer with a Cu Kα line of 0.1541 nm. Scanning electron microscopy (SEM; XL-30 ESEM FEG, Micro FEI Philips) and transmission electron microscopy (TEM; JEOL JEM-2100) were used to observe the morphologies and structures of the samples. Energy dispersive X-ray (EDX) spectroscopy being attached to scanning electron microscopy (SEM) was used to analyze the composition of products. Fourier transform infrared (FT-IR) spectra were obtained on a Magna 560 FT-IR spectrometer with a resolution of 1 cm^{-1}. X-ray photoelectron spectroscopy (XPS) was performed on a VG-ESCALAB LKII instrument with a Mg Kα ADES ($h\nu$ = 1253.6 eV) source at a residual gas pressure below 10^{-8} Pa. The UV–vis diffuse reflectance (DR) spectra of the samples were recorded on a TU-1950 UV–Vis–NIR spectrophotometer. The specific surface areas of the products were measured with a Micromeritics ASAP-2020 instrument and analyzed by the Brunauer–Emmett–Teller (BET) method. Decay curves of the as-fabricated products were obtained on a FLS920 fluorescence lifetime spectrophotometer (Edinburgh Instruments, UK) under the excitation of a hydrogen flash lamp with the wavelength at 325 nm (nF900; Edinburgh Instruments).

2.3. Photocatalytic test

The photocatalytic activities of the as-fabricated SnS$_2$/g-C$_3$N$_4$ heterojunction nanosheets were evaluated by the degradation of target pollutants, including organic dyes (Rhodamine B (RhB) and

Methyl orange (MO)) and phenols (4-nitrophenol (4-NP)), under visible light irradiation, respectively. Typically, the as-fabricated photocatalysts were suspended into 100 mL of aqueous solution containing one of the above organic dyes or phenols with an initial concentration of 10 mg L^{-1}. The above suspension was stirred in the dark for 30 min to obtain a good dispersion and establish adsorption–desorption equilibrium between the above pollutants and the photocatalysts surface before the light irradiation. A 300-W Xe lamp (HSX-F300, Beijing NBET Technology Co. Ltd.) coupled with a cutoff filter (400 nm < λ < 780 nm) was used to provide the visible light (output density of ~300 mW/cm^2). During the visible light irradiation, 4 mL of the reaction solution were sampled at the given time intervals and centrifuged to remove the catalysts and were then analyzed by a TU-1950 UV–Vis–NIR spectrophotometer. The degradability of the above pollutants was represented by C/C_0, where C_0 and C denoted the main absorption peak intensities of the above pollutants (RhB at 553 nm, MO at 463 nm, and 4-NP at 317 nm) before and after photocatalytic reaction. Photocatalytic activity of several reference samples, including SnS$_2$ and g-C$_3$N$_4$ nanosheets, were also measured by the same method. The wavelength-dependent photocatalysis tests were carried out under the 300-W Xe lamp (HSX-F300, Beijing NBET Technology Co. Ltd.) with different bandpass filters (380 ± 10, 420 ± 10, 450 ± 10, 475 ± 10, 500 ± 10 nm) after 30 min of irradiation.

3. Results and discussion

Typical X-ray diffraction (XRD) patterns of the as-fabricated products are shown in Fig. 1. For the g-C$_3$N$_4$ nanosheets, two characteristic peaks appeared 13.2° and 27.4°, corresponding to
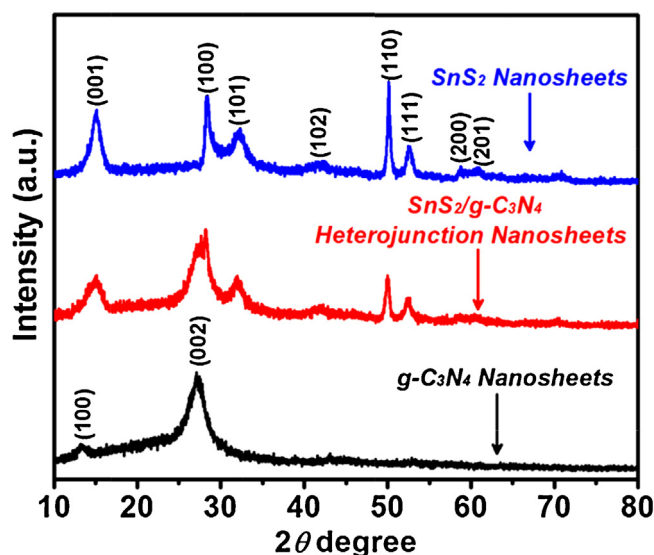

Fig. 1. XRD patterns of the as-fabricated SnS$_2$ nanosheets, SCHN5, and g-C$_3$N$_4$ nanosheets.

the periodic array of the in-planar tri-s-triazine and the inter-planar stacking of aromatic systems, can be perfectly indexed as the (1 0 0) and (0 0 2) diffraction planes of the graphite-like carbon nitride, respectively [14,20]. Moreover, all diffraction peaks on the XRD pattern of SnS$_2$ nanosheets can be ascribed to the 2T-type hexagonal berndtite SnS$_2$ (JCPDS, no. 23-677). The SnS$_2$/g-C$_3$N$_4$
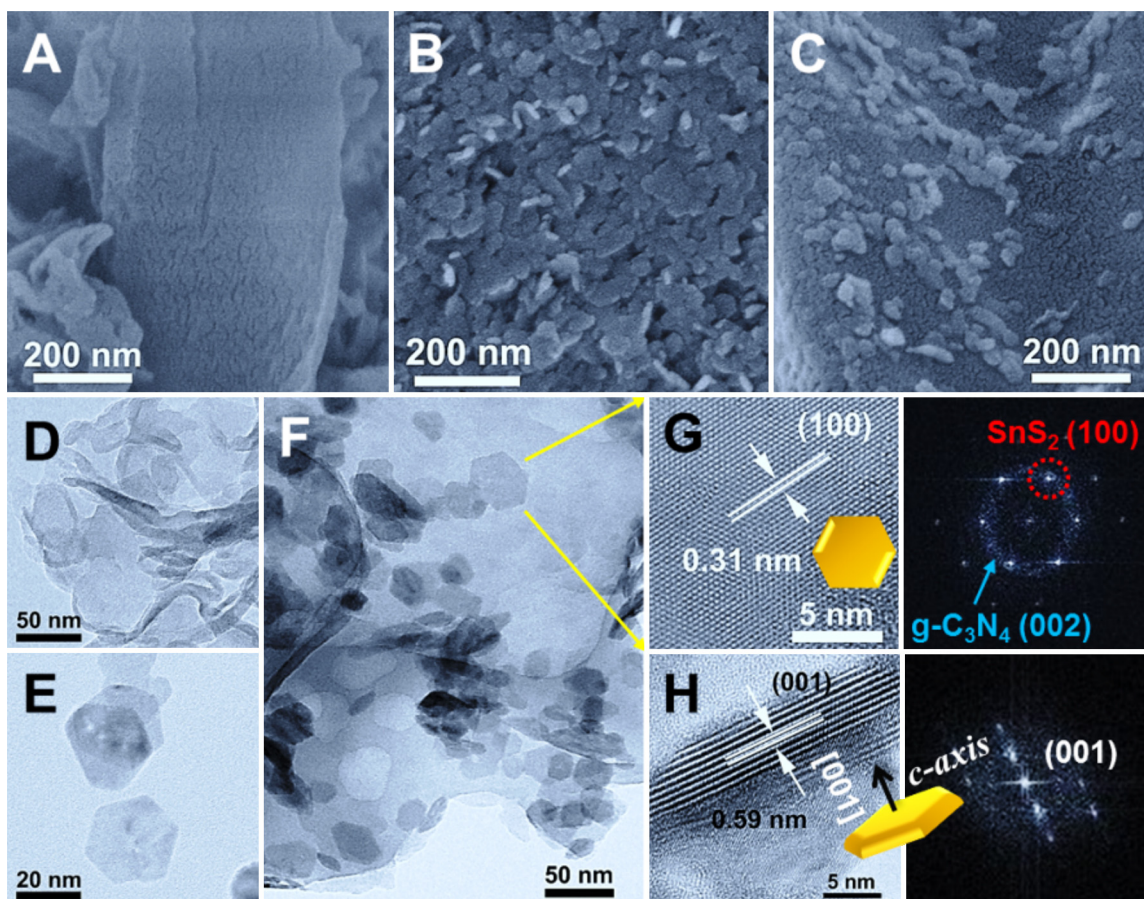

Fig. 2. SEM images of (A) g-C$_3$N$_4$ nanosheets, (B) SnS$_2$ nanosheets, and (C) SCHN5. TEM images of (D) g-C$_3$N$_4$ nanosheets, (E) SnS$_2$ nanosheets, and (F) SCHN5. (G and H) HRTEM images and the corresponding FFT patterns of SnS$_2$ nanosheets on the g-C$_3$N$_4$ nanosheets from image (F).

heterojunction nanosheets possess the feature peaks of both g-C_3N_4 and SnS_2 nanosheets, indicating that the SnS_2 nanosheets have been successfully loaded on g-C_3N_4 nanosheets through the ultrasonic dispersion method (Figure S1).

Scanning electron microscopy (SEM) and transmission electron microscopy (TEM) were used to observe the morphologies and microstructures of SnS_2/g-C_3N_4 heterojunction nanosheets along with SnS_2 and g-C_3N_4 nanosheets for the purpose of comparison. It is obvious that the g-C_3N_4 has a wrinkled sheet-like structure with relatively smooth surface (Fig. 2A and D). The single SnS_2 nanosheet presents a hexagonal structure with a lateral size of 40–70 nm and thickness of 4–8 nm. And, these SnS_2 nanosheets very easily aggregate to minimize their surface areas due to the higher surface energy (Fig. 2B and E). However, after ultrasonic treatment in the presence of g-C_3N_4 nanosheets as the substrates, the SnS_2 nanosheets with good dispersion are uniformly lying flat on the g-C_3N_4 nanosheet surface (Fig. 2C and F), indicating that the surface energy of SnS_2 nanosheets might be lowered down by the g-C_3N_4 nanosheet through a chemical interaction. Fig. 2G displays the high resolution TEM (HRTEM) image of the top view of the SnS_2 nanosheet loaded on the g-C_3N_4 nanosheet surface. It can be seen that the interplanar distance of 0.31 nm is in agreement with the d-spacing of (1 0 0) planes of the hexagonal SnS_2. Importantly, the corresponding Fast Fourier Transform (FFT) pattern reveals the simultaneous presence of the SnS_2 (1 0 0) and g-C_3N_4 (0 0 2) planes, further confirming the formation of the SnS_2/g-C_3N_4 heterojunction nanosheets. Meanwhile, the HRTEM image of the side view of the SnS_2 nanosheet with the thickness of ~8 nm is given in Fig. 2H. It can be found that the interplanar spacing value of 0.59 nm is consistent with the d-spacing of the (0 0 1) planes of the hexagonal SnS_2. And, its Fast Fourier Transform (FFT) pattern shows strong reflections associated with (0 0 1) planes, demonstrating that the SnS_2 layers are stacked along the [0 0 1] direction enforced by van der Waals interactions. Based on the above analyses, we believe that the ultrathin hexagonal SnS_2 nanosheets with a single crystalline
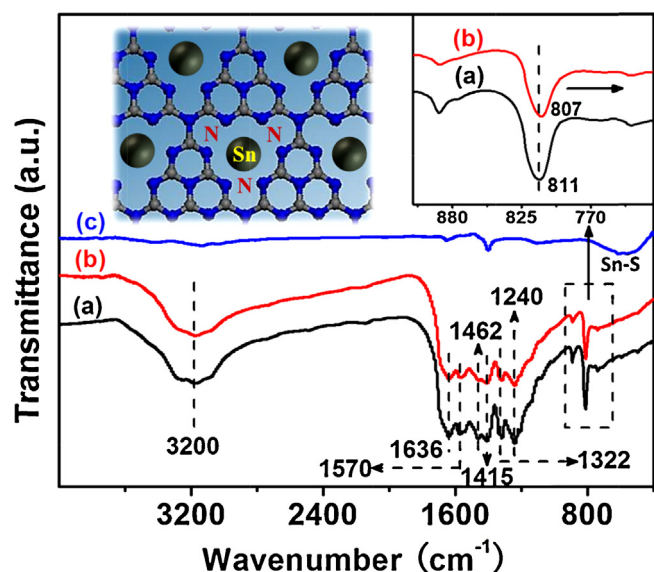
Fig. 3. FT-IR spectra of (a) g-C_3N_4 nanosheets, (b) SCHN5, and (c) SnS_2 nanosheets. The insert is the schematic diagram of the interaction between "nitrogen pots" of g-C_3N_4 and Sn species of SnS_2.

structure are horizontally loaded on the polycrystalline g-C_3N_4 nanosheets surface.

To investigate in-depth the atomic structure of SnS_2/g-C_3N_4 heterojunction nanosheets, the Fourier transform infrared (FT-IR) spectra were carried out. As observed in Fig. 3a, a series of peaks located between 1200 cm^{-1} and 1650 cm^{-1} are attributed to the typical stretching vibration modes of the CN heterocycles, while the peak centered at 3200 cm^{-1} is indicative of NH stretching vibration modes [19,23]. Additionally, the characteristic peak at 811 cm^{-1}, belonging to the stretching vibration modes of s-triazine ring unit
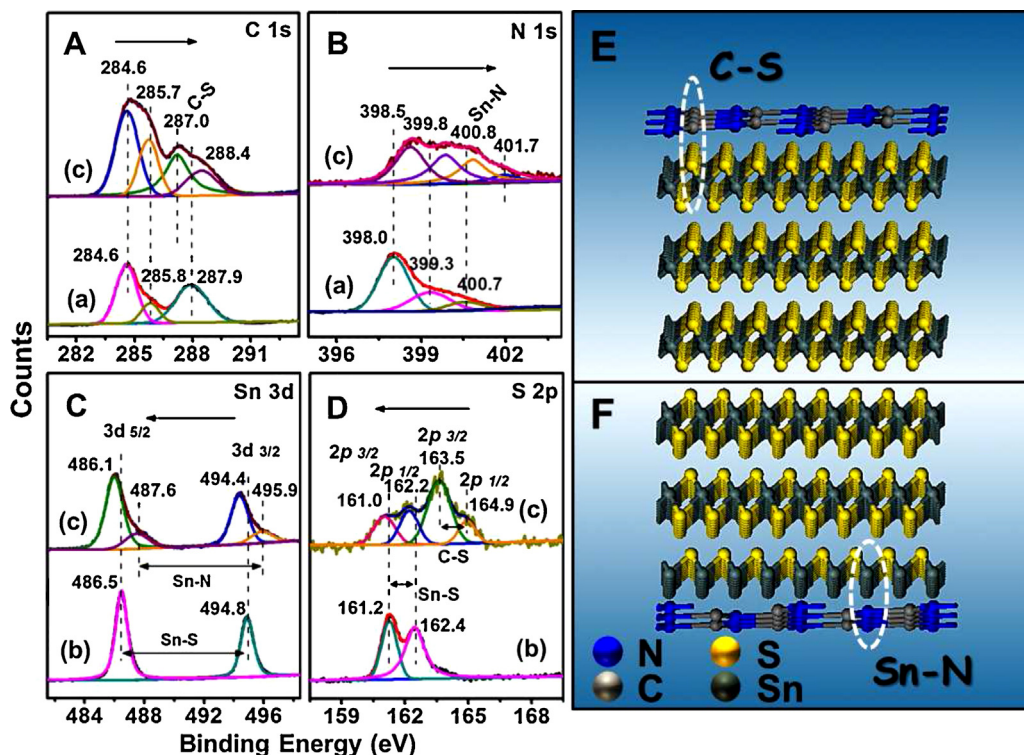
Fig. 4. XPS spectra of the as-fabricated products: (A) C 1s core-level spectra; (B) N 1s core-level spectra; (C) Sn 3d core-level spectra; (D) S 2p core-level spectra. (a) g-C_3N_4 nanosheets; (b) SnS_2 nanosheets; (c) SCHN5; (E) and (F) shows the schematic diagram of the possible bonding configurations between SnS_2 and g-C_3N_4 nanosheets.

[19,23], can be also found. In the case of SnS_2 nanosheets, a broad band peaked at 545 cm^{-1} is originated to the vibration of Sn-S bands (Fig. 3c) [24]. However, this feature band is difficult to distinguish on the curve of SnS_2/g-C_3N_4 heterojunction nanosheets due to the low content of SnS_2 nanosheets (Fig. 3b). Note that, after introducing the SnS_2 nanosheets, the characteristic peak from the s-triazine ring vibration of g-C_3N_4 nanosheets is shifted to 807 cm^{-1}, indicating that there might be some interactions between the "nitrogen pots" of g-C_3N_4 and Sn species of SnS_2.

X-ray photoelectron spectroscopy (XPS) analysis was employed to determine the chemical composition and bonding configuration of the as-fabricated products. As observed in Fig. 4A, the three main characteristic peaks of C 1s core-level of g-C_3N_4 nanosheets, corresponding to sp^2 C—C bonds of graphitic carbon (284.6 eV), sp^3-coordinated carbon bonds (285.8 eV), and sp^2-bonded carbon (N—C=N) in the s-triazine rings (287.9 eV) [20,21,23], can be detected on the curve of SnS_2/g-C_3N_4 heterojunction nanosheets. However, the peak relating to the N—C=N bonds of g-C_3N_4 is shifted to the higher binding energy side after loading SnS_2 nanosheets. In addition, a new peak with the binding energy at around 288.4 eV is observed, which may be ascribed to the formation of sp^3 C—S bond between g-C_3N_4 and SnS_2 nanosheets interface [27]. Fig. 2B displays the N 1s core-level spectra of SnS_2/g-C_3N_4 heterojunction nanosheets in comparison to g-C_3N_4 nanosheets. It is clear that, when forming the heterojunction, the N 1s feature peaks originated from sp^2-bonded N (C—N=C) (398.0 eV), tertiary nitrogen N-(C)$_3$ groups (399.3 eV), and amino groups (C-N-H) (400.7 eV) of g-C_3N_4 nanosheets [20,21,23] also shift toward the higher binding energy side. Interestingly, a new peak located at 400.8 eV can be seen on the N 1s core-level spectra of SnS_2/g-C_3N_4 heterojunction nanosheets, which may be related to the Sn—N bonds as mentioned in FI-IR spectra [28,29]. In contrast, the Sn 3d$_{5/2}$ and Sn 3d$_{3/2}$ peaks of SnS_2 nanosheets appeared at 486.5 eV and 494.8 eV [24,25], respectively, are higher than the corresponding binding energy of SnS_2/g-C_3N_4 heterojunction nanosheets (Fig. 4C). And, two weak peaks attributed to the Sn—N bonds are found at the Sn 3d core-level of heterojunction nanosheets [28,29], further indicating the possible bonding configuration of Sn—N on the heterojunction interface (Fig. 4F). Meanwhile, the S 2p peaks of SnS_2 nanosheets, reflecting to S—Sn bond [24,25], are also changed to the low binding energy side, when coupling with g-C_3N_4 nanosheets. Moreover, the formation of S—C bonds between the heterojunction interfaces can be further demonstrated by the two obvious peaks appeared at the higher binding energy side of S 2p spectrum of heterojunction nanosheets [30]. According to the literature, the binding energy shifts occurring on the XPS spectra in our work can be explained by the electron transfer between the SnS_2 and g-C_3N_4 nanosheets due to their different electron concentration [31,32]. Besides, there are two possible bonding configurations at the heterojunction interface, because the surface defects may induce different surface atomic on the SnS_2 nanosheets, as shown diagrammatically in Fig. 4E and F.

The optical properties of g-C_3N_4 nanosheets, SnS_2 nanosheets and SnS_2/g-C_3N_4 heterojunction nanosheets were revealed by the UV–vis diffuse reflectance (DR) spectra (Fig. 5). As expected, the g-C_3N_4 nanosheets exhibit an absorption edge at 450 nm, corresponding to the band gap of ~2.7 eV [20,21,23]. The SnS_2 nanosheets with the band gap around 2.48 eV show a light absorption region nearly in the entire visible light spectrum, which is similar with our previous results [24]. The SnS_2/g-C_3N_4 nanosheets present the hybrid absorption features of SnS_2 and g-C_3N_4 nanosheets. Furthermore, the absorption edges of SnS_2 nanosheets become more evident with the increase of SnS_2 nanosheet content in the heterojunction nanosheets (Figure S3). Furthermore, a Brunauer–Emmett–Teller (BET) analysis shown in Figure S4 reveals that the specific surface area of the 5.0 wt.% SnS_2/g-C_3N_4 heterojunction nanosheets is about 107.0 m^2/g, which is similar to that of

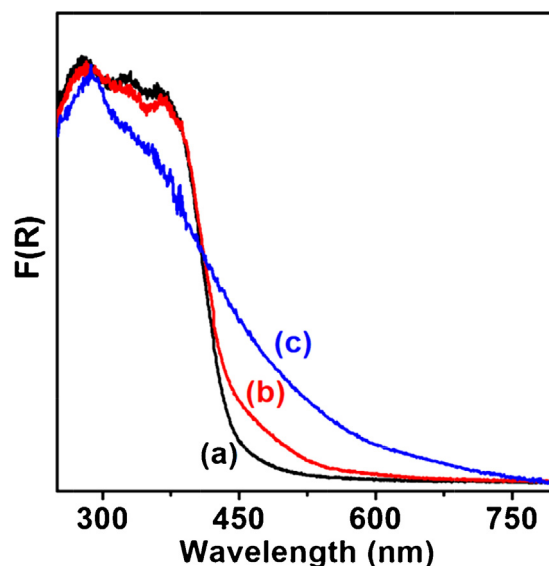**Fig. 5.** UV–vis absorption spectra of the (a) g-C_3N_4 nanosheets, (b) SCHN5, and (c) SnS_2 nanosheets, which are converted from diffuse reflectance spectra by means of the Kubelka–Munk function.

pure g-C_3N_4 nanosheets (112.4 m^2/g). The higher BET value implies the more active sites for the photocatalytic reaction.

The photocatalytic activities of the as-fabricated SnS_2/g-C_3N_4 heterojunction nanosheets were evaluated through the organic dyes (RhB and MO) and phenols (4-NP) degradation under visible light irradiation. Control experiments in the absence of either light irradiation or the as-fabricated photocatalysts showed no appreciable degradation of the above organic dyes or phenols (Figure S5). Fig. 6A presents a comparison of the photocatalytic degradation curves of g-C_3N_4 nanosheets, SnS_2 nanosheets and SnS_2/g-C_3N_4 heterojunction nanosheets. It is indicated that the SnS_2 content has a significant influence on the photocatalytic activity of g-C_3N_4 nanosheets. In the case of pure g-C_3N_4 nanosheets, only ~93.1% of RhB can be decomposed after visible light irradiation for 60 min. However, in the presence of SnS_2 nanosheets, the photoactivities of g-C_3N_4 nanosheets are remarkably enhanced. The photoactivities are also higher than that of pure SnS_2 nanosheets which only show ~80.2% degradation rate of RhB after irradiation for 60 min. In particular, the optimal heterojunction photocatalysts, SCHN5, can remove ~99.8% of RhB after only 20 min of visible light irradiation. These results suggest that the photosynergistic effect of SnS_2/g-C_3N_4 heterojunction can effectively enhance the photocatalytic activity of g-C_3N_4 nanosheets through the photoinduced interfacial charge transfer. For a better comparison of the photocatalytic efficiency of the above photocatalysts, the kinetic analyses of degradation of RhB are given in Fig. 6B through a pseudo-first-order reaction model [33,34]: $\ln(C_0/C) = K_{app}t$, where K_{app} is the apparent first-order rate constant (min^{-1}); t is the visible light irradiation time. It can be seen that the linearity between $\ln(C_0/C)$ and time are good for all the photocatalysts, implying that the photocatalytic degradation of RhB in aqueous suspensions can be described by pseudo-first-order reaction dynamics. As observed in Fig. 6C, the apparent rate constant of the heterojunction nanosheets increases with increasing the SnS_2 nanosheet contents from 0.5 wt.% to 5.0 wt.%. Nevertheless, when the SnS_2 nanosheet content is higher than 5.0 wt.%, a further increase in SnS_2 content causes a rapid decrease in the apparent rate constant. This decrease suggests the reduction of photocatalytic activity for the heterojunction nanosheets, mainly owing to the reduction light absorption of g-C_3N_4 nanosheets shielded by SnS_2 nanosheets, as shown in Figure S2F. The recycling experiment of RhB photodegradation
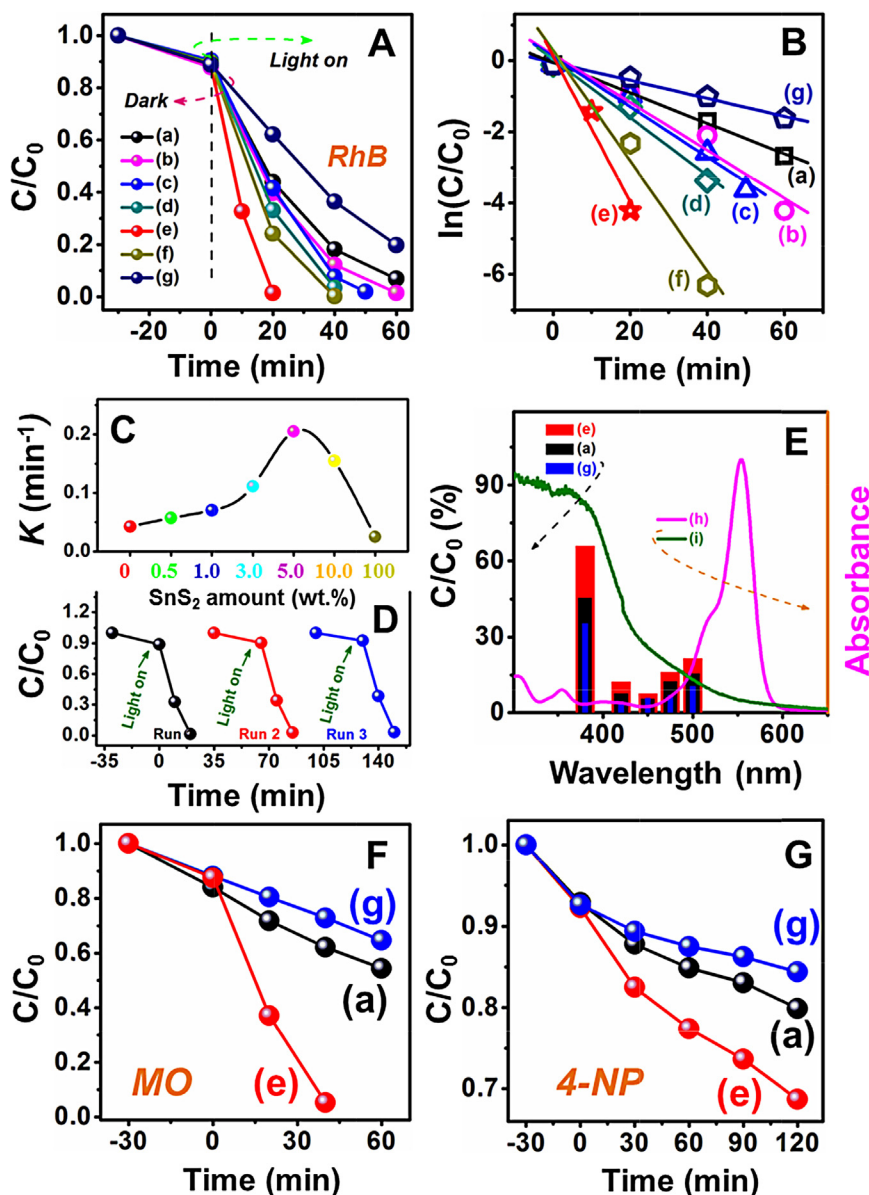
Fig. 6. Photocatalytic degradation curves of (A) RhB, (F) MO, and (G) 4-NP over the as-fabricated products under visible light irradiation (C_0 = 10 mg L^{-1}; photocatalyst: 10 mg for RhB and MO degradation and 50 mg for 4-NP degradation, respectively; C and C_0 stand for the remnants and initial concentration of the above target pollutants, respectively). (B) Kinetic linear simulation curves of RhB photocatalytic degradation over the as-fabricated products. (C) The comparison of apparent rate constant for the different products in the RhB photodegradation. (D) Photocatalytic activity of SCHN5 for the degradation of RhB with three times of cycling uses; (E) the UV–vis absorption spectra of (h) SCHN5 and (i) RhB aqueous solution, and the wavelength-dependent activities for photocatalytic degradation of RhB over the as-fabricated products (after visible light irradiation for 30 min): (a) g-C$_3$N$_4$ nanosheets; (b) SCHN0.5; (c) SCHN1; (d) SCHN3; (e) SCHN5; (f) SCHN10; (g) SnS$_2$ nanosheets.

indicates good stability of the heterojunction photocatalyst during the photocatalytic reaction (Fig. 6D). Moreover, the XRD pattern of heterojunction photocatalyst after photocatalytic reaction can further confirm this result (Figure S6).

As we know, the dye self-sensitized process can occur on the visible light photocatalysis [35]. In order to further investigate the photocatalytic activities of heterojunction nanosheets, we carried out the wavelength dependence of the photocatalysis tests. As shown in Fig. 6E, all the photocatalysts exhibit obviously photocatalytic activities, among which the SCHN5 shows the highest photodegradation ratio after irradiation for 30 min. Meanwhile, the photodegradation ratio of SCHN5 correlates well with its absorption spectrum as the excitation wavelength is lower than 475 nm. However, when we use the longer wavelength to initiate the photoreaction, the photodegradation ratio started to depend on the

absorption spectrum of RhB, implying the dye self-sensitized process dominates the photocatalysis at this condition. Based on the above results, we can conclude that the photosynergistic effect driven by the SnS$_2$/g-C$_3$N$_4$ heterojunction plays the key role on the enhancement of photocatalytic activity through the interfacial charge transfer, in particular, as the excitation energy is higher than the absorption edge of the heterojunction. Besides, we also studied the photocatalytic activities of SCHN5 for the degradation of MO and 4-NP, respectively, because these target pollutants have more stable structure and poor self-sensitization [36,37]. As shown in Fig. 6F and G, the photodegradation ratios of MO and 4-NP are about ~95.0% and ~31.3% for the SCHN5 under visible light irradiation for 40 and 120 min, respectively. These photodegradation ratios are much higher than the corresponding degradation ratios of above pollutants when using pure g-C$_3$N$_4$ nanosheets (MO: ~45.5%; 4-NP:
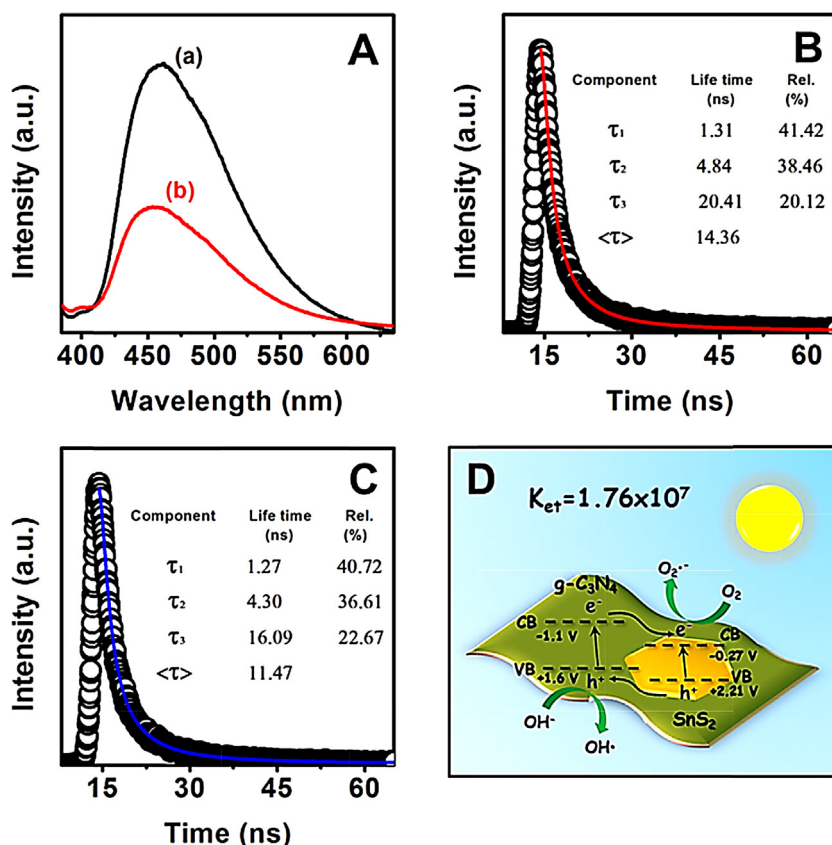
Fig. 7. (A) Steady-state PL spectra of (a) g-C_3N_4 nanosheets and (b) SCHN5. Time-resolved transient PL decay of (B) g-C_3N_4 nanosheets and (C) SCHN5. (D) Schematic diagram showing the photoinduced interfacial charge transfer and photocatalytic reaction process of SnS_2/g-C_3N_4 heterojunction nanosheet.

~20.1%) and SnS_2 nanosheets (MO: ~35.4%; 4-NP: ~15.6%) (Figure S7). Thus, we believe that the photoinduced interfacial charge transfer is responsible to the enhanced photocatalytic activities of SnS_2/g-C_3N_4 heterojunction nanosheets.

To provide further evidence on the photoinduced interfacial charge transfer process, the steady-state and transient photoluminescence (PL) spectroscopy of SnS_2/g-C_3N_4 heterojunction nanosheets were studied in comparison with those of pure g-C_3N_4 nanosheets. As shown in Fig. 7A, the pure g-C_3N_4 nanosheets exhibit a strong emission peak at around ~450 nm. However, when 5.0 wt.% SnS_2 nanosheets were present on the surface of g-C_3N_4 nanosheets, the intensity of this emission peak dropped significantly, suggesting that the recombination of photoinduced charge carrier is inhibited greatly by the interfacial charge transfer between g-C_3N_4 and SnS_2 nanosheets. This process was then understood by the time-resolved transient PL spectroscopy. As can be seen in Fig. 7B and C, the emission decay data can be fitted by triexponential kinetics for which three components are derived. In the case of SCHN5, the emission lifetimes of all components are shorter than the corresponding lifetimes of g-C_3N_4 nanosheets ($\tau_1 = 1.27$ ns, $\tau_2 = 4.30$ ns, and $\tau_3 = 16.09$ ns for SCHN5 versus $\tau_1 = 1.31$ ns, $\tau_2 = 4.84$ ns, and $\tau_3 = 20.41$ ns for g-C_3N_4 nanosheets). Moreover, an overall comparison of the emission decay behavior is deduced by the intensity-average lifetimes through the following equation [38]:

$$\langle \tau \rangle = \frac{A_1 \tau_1^2 + A_2 \tau_2^2 + A_3 \tau_3^2}{A_1 \tau_1 + A_2 \tau_2 + A_3 \tau_3}.$$

The results show that, after introducing the SnS_2 nanosheets, the $\langle \tau \rangle$ value of g-C_3N_4 nanosheets is decreased from 14.36 ns to 11.47 ns. This observed shortening of emission lifetime indicates the

emergence of a nonradiative pathway from the electronic interaction between g-C_3N_4 and SnS_2 nanosheets [39]. On the basis of the energy band structures of these two semiconductors, we propose that the photoinduced electron transfer occurs from the conduction band (CB) of g-C_3N_4 to the CB of SnS_2 nanosheets, because the CB of g-C_3N_4 nanosheets (~−1.1 V vs. NHE) is more negative than that of SnS_2 nanosheets (~−0.27 V vs. NHE) [20,21,23,24]. This assumption can be also confirmed by the emission quenching of g-C_3N_4 observed for SCHN5. If the photoinduced electron transfer from g-C_3N_4 to SnS_2 nanosheets is the predominant process that results in the emission quenching of g-C_3N_4, we can estimate the electron-transfer rate constant (k_{et}) by the expression [40]:

$$k_{et}(\text{g-}C_3N_4 \rightarrow SnS_2) = \frac{1}{\langle \tau \rangle_{(\text{g-}C_3N_4/SnS_2)}} - \frac{1}{\langle \tau \rangle_{(\text{g-}C_3N_4)}},$$

approximately $1.76 \times 10^7\,S^{-1}$. Owing to the effective electron transfer from g-C_3N_4 to SnS_2 nanosheets, the photoinduced holes on the valence band (VB) of SnS_2 nanosheets (~+2.21 V vs. NHE) would transfer to the VB of g-C_3N_4 nanosheets (~+1.6 V vs. NHE) at their heterojunction interface [20,21,23,24]. Therefore, the separation efficiency of photoinduced charge carriers is remarkably improved by the photosynergistic effect of SnS_2/g-C_3N_4 heterojunction through the photoinduced interfacial charge transfer (Fig. 7D). During the photocatalysis process, the photoinduced holes are ultimately trapped by surface hydroxyl groups (or H_2O) at the photocatalyst surface to yield OH• radicals. Meanwhile, the dissolved oxygen molecules react with the electrons to produce superoxide radical anions, $O_2^{\bullet-}$, which on protonation generates the hydroperoxy, $HO_2^{\bullet}$, radicals, forming hydroxyl radical OH•, which is a strong oxidizing agent for decomposing the organic dye

[41,42]. As such, the effective charge separation at the heterojunction interface can lead to the enhanced photocatalytic activities.

4. Conclusions

In summary, a series of SnS_2/g-C_3N_4 heterojunction nanosheets with different contents of SnS_2 have been successfully fabricated through a facile ultrasonic dispersion method. The ultrathin hexagonal SnS_2 nanosheets horizontally loaded on g-C_3N_4 nanosheets lead to considerable enhancement on the photocatalytic activities for the degradation of organic dyes and phenols under visible light irradiation as compared to pure g-C_3N_4 and SnS_2 nanosheets. The improved photoactivities are attributed to the effective charge transfer across the heterojunction interface, as evidenced by the electron microscopic analyses, steady-state and time-resolved transient photoluminescence decay studies. Our present work provides a new insight on developing 2D/2D heterojunction photocatalysts with effective charge separation for the efficient photodegradation of organic pollutants from wastewater.

Appendix A. Supplementary data

Supplementary data associated with this article can be found, in the online version, at http://dx.doi.org/10.1016/j.apcatb.2014.08.013.

References

[1] M.R. Hoffmann, S.T. Martin, W. Choi, D.W. Bahnemann, Chem. Rev. 95 (1995) 69–96.
[2] A. Fujishima, K. Honda, Nature 238 (1972) 37–38.
[3] D.M. Todorovic, M.D. Rabasovic, D.D. Markushev, M. Franko, U.L. Stangar, Sci. China Phys. Mech. Astron. 56 (2013) 1285–1293.
[4] X. Yang, Y. Qu, Y. Fan, X. Liu, Sci. China Phys. Mech. Astron. 55 (2012) 14–18.
[5] X. Chen, L. Liu, P.Y. Yu, S.S. Mao, Science 331 (2011) 749–750.
[6] Q. Jia, W. Que, X. Qiu, P. Zhong, J. Chen, Sci. China Phys. Mech. Astron. 55 (2012) 1158–1162.
[7] X. Zhao, H. Lin, Y. Liu, X. Li, P. Yang, H. Chen, G. Wang, J. Li, Sci. China Phys. Mech. Astron. 55 (2012) 1203–1209.
[8] J.W. Tang, Z.G. Zou, J.H. Ye, Angew. Chem. Int. Ed. 43 (2004) 4463–4466.
[9] D. Wang, T. Kako, J. Ye, J. Am. Chem. Soc. 130 (2008) 2724–2725.
[10] L. Zhao, X. Chen, X. Wang, Y. Zhang, W. Wei, Y. Sun, M. Antonietti, M.-M. Titirici, Adv. Mater. 22 (2010) 3317–3321.
[11] X. Wang, K. Maeda, A. Thomas, K. Takanabe, G. Xin, J.M. Carlsson, K. Domen, M. Antonietti, Nat. Chem. 8 (2009) 76–80.
[12] F. Dong, Z. Zhao, T. Ni, W. Zhang, Y. Sun, W.-K. Ho, ACS Appl. Mater. Interfaces 5 (2013) 11392–11401.
[13] Y. Tian, B. Chang, J. Lu, J. Fu, F. Xi, X. Dong, ACS Appl. Mater. Interfaces 5 (2013) 7079–7085.
[14] X. Wang, X. Chen, A. Thomas, X. Fu, M. Antonietti, Adv. Mater. 21 (2009) 1609–1612.
[15] C. Pan, J. Xu, Y. Wang, D. Li, Y. Zhu, Adv. Funct. Mater. 22 (2012) 1518–1524.
[16] H. Xu, J. Yan, Y. Xu, Y. Song, H. Li, J. Xia, C. Huang, H. Wan, Appl. Catal. B: Environ. 129 (2013) 182–193.
[17] N. Cheng, J. Tian, Q. Liu, C. Ge, A.H. Qusti, A.M. Asiri, A.O. Al-Youbi, X. Sun, ACS Appl. Mater. Interfaces 5 (2013) 6815–6819.
[18] S. Wang, D. Li, C. Sun, S. Yang, Y. Guan, H. He, Appl. Catal. B: Environ. 144 (2014) 885–892.
[19] L. Sun, X. Zhao, C.-J. Jia, Y. Zhou, X. Cheng, P. Li, L. Liu, W. Fan, J. Mater. Chem. 22 (2012) 23428–23438.
[20] S.-W. Cao, X.-F. Liu, Y.-P. Yuan, Z.-Y. Zhang, Y.-S. Liao, J. Fang, S.C.J. Loo, T.C. Sum, C. Xue, Appl. Catal. B: Environ. 147 (2014) 940–946.
[21] S. Cao, J. Yu, J. Phys. Chem. Lett. 5 (2014) 2101–2107.
[22] Q. Xiang, J. Yu, M. Jaroniec, J. Phys. Chem. C 115 (2011) 7355–7363.
[23] T. Li, L. Zhao, Y. He, J. Cai, M. Luo, J. Lin, Appl. Catal. B: Environ. 129 (2013) 255–263.
[24] Z. Zhang, C. Shao, X. Li, Y. Sun, M. Zhang, J. Mu, P. Zhang, Z. Guo, Y. Liu, Nanoscale 5 (2013) 606–618.
[25] Y.C. Zhang, Z.N. Du, K.W. Li, M. Zhang, D.D. Dionysiou, ACS Appl. Mater. Interfaces 3 (2011) 1528–1537.
[26] X. Li, J. Zhu, H. Li, Appl. Catal. B: Environ. 123–124 (2012) 174–181.
[27] A.D. Vogt, T. Han, T.P. Beebe, Langmuir 13 (1997) 3397–3403.
[28] Y. Wu, H. Liu, J. Zhang, F. Chen, J. Phys. Chem. C 113 (2009) 14689–14695.
[29] B. Zhou, S. Dong, H. Zhao, Y. Liu, P. Wu, J. Magn. Magn. Mater. 362 (2014) 14–19.
[30] J.F. Moulder, W.F. Stickle, P.E. Sobol, K.D. Bomben, in: J. Chastain (Ed.), Handbook of X-ray Photoelectron Spectroscopy, Perkin-Elmer Corp., New York, 1992.
[31] X.H. Li, H.Y. Xu, X.T. Zhang, Y.C. Liu, J.W. Sun, Y.M. Lu, Appl. Phys. Lett. 95 (2009) 191903(1–3).
[32] Z. Zhang, C. Shao, X. Li, C. Wang, M. Zhang, Y. Liu, ACS Appl. Mater. Interfaces 2 (2010) 2915–2923.
[33] M.S. Lee, S.S. Park, G.-D. Lee, C.-S. Ju, S.-S. Hong, Catal. Today 101 (2005) 283–290.
[34] C.S. Turchi, D.F. Ollis, J. Catal. 122 (1990) 178–192.
[35] L. Pan, J. Zou, X. Zhang, L. Wang, J. Am. Chem. Soc. 133 (2011) 10000–10002.
[36] E. Dvininov, U.A. Joshi, J.R. Darwent, J.B. Claridge, Z. Xu, M.J. Rosseinsky, Chem. Commun. 47 (2011) 881–883.
[37] N. Daneshvar, M.A. Behnajady, Y.Z. Asghar, J. Hazard. Mater. B 139 (2007) 275–279.
[38] Y.-C. Chen, Y.-C. Pu, Y.-J. Hsu, J. Phys. Chem. C 116 (2012) 2967–2975.
[39] Z. Bian, T. Tachikawa, W. Kim, W. Choi, T. Majima, J. Phys. Chem. C 116 (2012) 25444–25453.
[40] T.-T. Yang, W.-T. Chen, Y.-J. Hsu, K.-H. Wei, T.-Y. Lin, T.-W. Lin, J. Phys. Chem. C 114 (2010) 11414–11420.
[41] T. Aarthi, G. Madras, Ind. Eng. Chem. Res. 46 (2007) 7–14.
[42] K. Rajeshwar, M.E. Osugi, W. Chanmanee, C.R. Chenthamarakshan, M.V.B. Zanoni, P. Kajitvichyanukul, R. Krishnan-Ayer, J. Photochem. Photobiol. A: Chem. 9 (2008) 171–192.